Available online at www.sciencedirect.com
SCIENCE DIRECT
Journal of Colloid and Interface Science 295 (2006) 50–64
JOURNAL OF Colloid and Interface Science
www.elsevier.com/locate/jcis

Zn^{2+} and Sr^{2+} adsorption at the TiO_2 (110)–electrolyte interface: Influence of ionic strength, coverage, and anions

Z. Zhang [a,b,*], P. Fenter [a], L. Cheng [a], N.C. Sturchio [a,c], M.J. Bedzyk [b], M.L. Machesky [d], L.M. Anovitz [e], D.J. Wesolowski [e]

[a] *Environmental Research Division, Argonne National Laboratory, Argonne, IL 60439, USA*
[b] *Institute of Environmental Catalysis, Northwestern University, Evanston, IL 60208, USA*
[c] *University of Illinois at Chicago, Chicago, IL 60607, USA*
[d] *Illinois State Water Survey, Champaign, IL 61820, USA*
[e] *Oak Ridge National Laboratory, Oak Ridge, TN 37831, USA*

Received 9 June 2005; accepted 5 August 2005

Available online 8 September 2005

Abstract

The X-ray standing wave technique was used to probe the sensitivity of Zn^{2+} and Sr^{2+} ion adsorption to changes in both the adsorbed ion coverage and the background electrolyte species and concentrations at the rutile (α-TiO_2) (110)–aqueous interface. Measurements were made with various background electrolytes (NaCl, NaTr, RbCl, NaBr) at concentrations as high as 1 *m*. The results demonstrate that Zn^{2+} and Sr^{2+} reside primarily in the condensed layer and that the ion heights above the Ti–O surface plane are insensitive to ionic strength and the choice of background electrolyte (with <0.1 Å changes over the full compositional range). The lack of any specific anion coadsorption upon probing with Br^-, coupled with the insensitivity of Zn^{2+} and Sr^{2+} cation heights to changes in the background electrolyte, implies that anions do not play a significant role in the adsorption of these divalent metal ions to the rutile (110) surface. Absolute ion coverage measurements for Zn^{2+} and Sr^{2+} show a maximum Stern-layer coverage of $\sim$0.5 monolayer, with no significant variation in height as a function of Stern-layer coverage. These observations are discussed in the context of Gouy–Chapman–Stern models of the electrical double layer developed from macroscopic sorption and pH-titration studies of rutile powder suspensions. Direct comparison between these experimental observations and the MUltiSIte Complexation (MUSIC) model predictions of cation surface coverage as a function of ionic strength revealed good agreement between measured and predicted surface coverages with no adjustable parameters.

Keywords: Electrical double layer; Rutile; Adsorption; Oxide–aqueous interface; X-ray standing wave; Multisite complexation; Ionic strength

1. Introduction

The distribution of ions near a charged surface (i.e., the electrical double layer or EDL) is a well-known phenomenon at oxide–aqueous solution interfaces. The EDL plays an important role in many interfacial chemical reactions, including both industrial and natural processes, such as mineral dissolution/precipitation, water purification, and heterogeneous catalysis [1–3]. Various models have been developed to explain EDL macroscopic properties [4–11]. For instance, the recent application of the MUltiSIte Complexation (MUSIC) model to rutile surface-charging data has enabled prediction of ion coverages in the condensed and diffuse layers at oxide–aqueous interfaces, revealing insight into both the ion adsorption strength and the electrostatic potential profile at an interface [9,12,13]. Studies coupling complexation modeling with electrophoresis measurements have yielded new insights into the isoelectric point of rutile powders, leading to the conclusion that the zeta plane height corresponds to the Debye length [14]. However, many fundamental aspects of these models have not been tested, because only a few direct measurements of ion distributions in the EDL have been reported [15–17]. For instance, the various surface complexation models (SCMs) implicitly assume that

* Corresponding author. Fax: +1 630 252 5498.
E-mail address: zhanzhang@anl.gov (Z. Zhang).

0021-9797/$ – see front matter
doi:10.1016/j.jcis.2005.08.018

the condensed-layer ion height is invariant with changes in the solution conditions (e.g., ion concentration and ionic strength) [8–10,18].

X-ray studies, including crystal truncation rod (CTR) and extended X-ray absorption fine structure (EXAFS) measurements, have already revealed some molecular-scale EDL features [19–28]. To date, the most direct probe of EDL distributions comes from X-ray standing wave (XSW) approaches, although only a few results have been reported, including total external reflection XSW (TER-XSW) results [15,16,29] and Bragg XSW measurements [20,30,31] at the mineral–water interface. TER-XSW probes the decay length of the diffuse-layer ion distribution [15,16], but it is insensitive to condensed-layer properties. On the other hand, an XSW generated by Bragg reflection typically has a period of a few angstroms, which is suitable for probing the condensed-layer height. This height is closely related to the distance between the 0-plane and the β-plane in the EDL [2,10], which is a critical parameter for modeling EDL structures and properties in most SCMs [9,10,13,32].

A few in situ X-ray measurements of condensed-layer ion heights have been made previously [20,25–28,30,31]. In particular, Sr^{2+}, Zn^{2+}, Y^{3+}, and Rb^{+} ion locations were measured at the rutile (110)–aqueous interface [31]. When this structure information is combined with computational studies of the rutile–water system using both ab initio methods [33,34] and molecular dynamics simulations [35,36], our understanding of the interactions of these ions with the rutile surface have been greatly extended.

Prior to this work, essentially no information is available on the systematic partitioning of ions between the condensed and the diffuse layers or the sensitivity of the EDL structure to changes in solution conditions. Here, we report additional results obtained by using the Bragg XSW technique to probe the sensitivity of Sr^{2+} and Zn^{2+} ion distributions at single-crystal rutile α-TiO_2 (110)–aqueous interfaces. Specifically, we show that the condensed-layer ion height of these divalent cations is insensitive to ion coverage and background electrolyte (including the choice of electrolyte and ionic strength), and we determine the saturation Stern-layer coverage of each ion. We find the Gouy–Chapman–Stern model to be suitable for describing the adsorption of Sr^{2+} and Zn^{2+} ions at the rutile (110)–aqueous interface, and we discuss partitioning of ions between the condensed and the diffuse layers.

2. Materials and methods

2.1. X-ray standing waves

The single-crystal Bragg XSW method is a powerful tool for probing adsorbate positions at the solid-water interface [37]. When an X-ray plane wave (Fig. 1A) is Bragg-diffracted from a single crystal lattice, an XSW is generated both above and below the crystal surface as a result of coherent superposition of the incident and the reflected X-ray beams [37–40]. The Bragg reflectivity and the X-ray fluorescence signal are measured simultaneously while the sample is rocked through the H^{th} ($=hkl$) Bragg reflection.

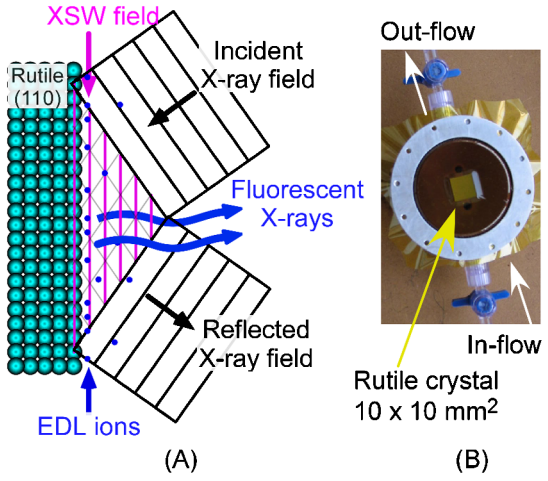

Fig. 1. (A) Schematic of the Bragg XSW experiment. (B) In situ sample cell.

The normalized fluorescence yield $Y(\theta)$ varies with respect to incident angle θ as

$$Y(\theta) = 1 + R(\theta) + 2\sqrt{R(\theta)}\, f_H \cos\bigl[v(\theta) - 2\pi P_H\bigr]. \tag{1}$$

Here, $R(\theta)$ is the reflectivity, and $v(\theta)$ is the phase between the reflected and the incident X-ray plane waves. Both $R(\theta)$ and $v(\theta)$ can be calculated directly for the known bulk crystal structure by using X-ray dynamical diffraction theory. P_H and f_H are the so-called "coherent position" and "coherent fraction" for the measured element, respectively; they are obtained directly from the experimental XSW data by using Eq. (1). These two parameters represent the phase and the amplitude of the H^{th} Fourier component of the fluorescing species' spatial distribution [37,41], or

$$f_H \exp[i2\pi P_H] = \mathbf{F}(\mathbf{H}) = \int \rho(\mathbf{r}) \exp[i\mathbf{H}\cdot\mathbf{r}]\, \mathrm{d}r. \tag{2}$$

Here $|\mathbf{H}| = 2\pi/d_H$, with d_H both the period of the XSW field and the d-spacing of the H^{th} Bragg diffraction planes; and $\rho(\mathbf{r})$ represents the normalized three-dimensional (3-D) distribution profile of the fluorescent species; that is,

$$\int \rho(\mathbf{r})\, \mathrm{d}\mathbf{r} = 1. \tag{3}$$

As demonstrated recently, the complete density profile (projected into the substrate crystallographic unit cell) can be obtained from the inverse statement of Eq. (2) through a discrete Fourier summation with a full set of the H^{th} Fourier components, because no phase information is lost in the XSW approach [30,37,41,42]. Here, we instead perform XSW measurements by using the rutile (110) reflection as a function of solution conditions in order to obtain insight into systematic changes in EDL properties. Consequently, we must discuss the interpretation of the XSW parameters, P_H and f_H.

A complete discussion of the relationship between P_H and f_H and the ion distributions for the Gouy–Chapman (GC) and the Gouy–Chapman–Stern (GCS) models is in Appendix A. Both P_H and f_H are unitless quantities ranging between 0

and 1. When the fluorescing ion has a unique projected location within the substrate's primary crystallographic unit cell, $P_H = \delta_H/d_H$, where δ_H is the height of the ion from the unit cell origin along the diffraction plane normal direction. The coherent fraction, f_H, is a measure of the distribution of the ions around the position defined by P_H. In general, f_H can be described as the product of three factors,

$$f_H = a_H C D_H, \tag{4}$$

where a_H is the "geometry factor," C is the "ordered fraction," and D_H is the Debye–Waller factor. The geometry factor accounts for the contributions from ions at discrete positions;

$$a_H = \left|\sum_j \Theta_j \exp(i\mathbf{H}\cdot\mathbf{r}_j)\right| \Big/ \left(\sum_j \Theta_j\right); \tag{5}$$

Θ_j is the coverage (2-D number density projected onto the crystal surface) of specifically adsorbed condensed-layer ions at position $\mathbf{r}_j$; $\sum_j \Theta_j \equiv \Theta_C$, therefore, is the total condensed-layer coverage. When the position of the condensed-layer ion is unique along $\mathbf{H}$ direction, $a_H = 1$.

The ordered fraction corresponds to the fraction of all fluorescing ions (with equivalent coverage Θ_{tot}) in ordered sites. As shown in Appendix A, the diffuse-layer ions (having coverage Θ_D) are sufficiently distributed to appear incoherent in the Bragg XSW measurements. Other incoherent contributions to fluorescence include ions in the bulk solution, multinuclear/polymeric species, and any other accumulations of fluorescing ions in the beam path that are unrelated to the ideal (110) surface, such as on dust particles, on defects and step edges, on the Kapton window, and on surface organic films (collectively referred to as Θ_{other}). Consequently, the ordered fraction can be written as

$$C = \Theta_C/\Theta_{\text{tot}} = \Theta_C/(\Theta_C + \Theta_D + \Theta_{\text{other}}). \tag{6}$$

The Debye–Waller factor accounts primarily for thermal vibrations of the fluorescing ions, and more generally for any contribution to the elemental distribution having a Gaussian distribution [37,40]. With a root-mean-squared width σ_H, this leads to

$$D_H = \exp\left[-|\mathbf{H}|^2\sigma_H^2/2\right] = \exp\left[-2\pi^2\sigma_H^2/d_H^2\right]. \tag{7}$$

For chemically bound species, $\sigma_H \approx 0.1$ Å. Consequently, for a typical Bragg reflection where $d_H \sim 3$ Å, $D_H \approx 1$. Therefore, we can describe the coherent fraction of EDL ions as $f_H \approx a_H C$. For ions having a unique adsorption site, such as the previously determined Sr^{2+}, Y^{3+}, and Rb^+ ions at the rutile (110)–aqueous interface, $a_{110} = 1$. In these cases the measured coherent fraction is directly related to the fraction of EDL ions that are ordered in discrete sites at the interface. On the other hand, Zn^{2+} ions are identified at two distinct adsorption sites, whose measured coherent position is the coherently averaged height of the two sites. With a_{110} estimated to be 0.9, the measured coherent fraction can be written as $f_{110} \approx 0.9C$. (See Appendix A for more details.)

2.2. Experimental details

The XSW measurements were preformed primarily at beamline X15A at the National Synchrotron Light Source (NSLS), Brookhaven National Laboratory, and at beamline 12-ID-D (BESSRC-CAT) at the Advanced Photon Source (APS), Argonne National Laboratory. Measurements at X15A used X-ray energy at 17.0 keV for both Zn^{2+} and Sr^{2+}, with a typical beam size of 0.1×0.4 mm^2. Measurements at beamline 12-ID-D were carried out at 11.5 keV for Zn^{2+} and 17.5 keV for Sr^{2+}, with a typical beam size of 0.02×0.1 mm^2. Si or Ge fluorescence detectors were used to collect characteristic X-ray fluorescence signals from the crystal surface at a takeoff angle ∼6°. Care was taken to choose a beam spot where the rocking curve was closely matched to the theoretical prediction for a perfect crystal. Experiments were performed on spots where the measured absolute peak reflectivity was >70% (as compared to the theoretical peak reflectivity of ∼90% under these conditions for a perfect rutile single crystal), and the rocking curve width was less than 1.5ω, where ω is the Darwin width of the rocking curve expected on the basis of dynamical diffraction theory, including dispersion due to the specific monochromator used.

The measurements were performed in situ in a thin-film cell as shown in Fig. 1B. The solution composition was changed by injecting solution into the cell through the in-flow tube and exposing the sample to an aqueous solution ∼1 mm thick, held between the Kapton window and the sample surface. Full equilibration between the sample surface and the solution was ensured by waiting 10 to 15 min after each injection and by repeating the procedure at least three times for each new solution. Adsorption was rapid with respect to exposure time. Under these experimental conditions (with ion concentrations of 10^{-5} or 10^{-4} m), the total volume of solution passed over the crystal surface contained a substantial excess of ions with respect to the available surface sites, suggesting that the measurements should represent the equilibrium ion distribution. A convenient unit for ion coverage is the monolayer (ML). Here, 1 ML is defined as 1 ion per TiO_2 (110) surface unit cell. With a surface unit cell area of $6.50 \times 2.96 = 19.24$ Å^2, 1 ML $= 5.3 \times 10^{14}$ ions/cm^2 $= 8.8$ μmol/m^2.

Before each XSW measurement, the excess solution between the Kapton window and the sample surface was minimized by applying a small negative pressure, and the cell was sealed to maintain a minimal solution thickness of ∼2 μm during the XSW measurements. The cell was held in a controlled atmosphere of pure N_2 gas to minimize any diffusion of reactive atmospheric gases (e.g., CO_2) through the Kapton window.

Sample preparation is critical for ion adsorption measurements. Rutile was chosen for these studies because it has been studied extensively [43,44]. Polished rutile (110) single crystals ($10 \times 10 \times 1$ mm^3) were obtained from Princeton Scientific with a typical miscut of ⩽0.1° with respect to the (110) crystallographic plane. The crystal surface was treated as described previously [31]. Atomic force microscopy (AFM) images of rutile samples as received from the manufacturer (Fig. 2A) and after the treatment (Fig. 2B) revealed that although the original surface was very rough, atomically flat terraces (>0.1 μm

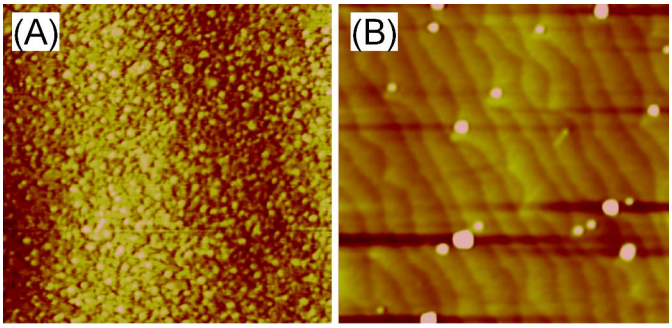

Fig. 2. Atomic force microscopy images of the rutile (TiO_2) (110) surface (A) as received and (B) after annealing in air at 1000 °C. Both images are 2 × 2 μm in area. The treated surface shows atomic-scale flat terraces separated by steps the height of a single unit cell.

across) separated by steps with the height of a single unit cell (3.25 Å) were present after the treatment. CTR measurements of the treated surface [31] showed no evidence of surface reconstruction observed for oxygen-depleted surfaces prepared by sputtering and annealing in high vacuum [44–46].

The composition, ionic strength, and calculated Debye length for each solution discussed below are listed in Tables 1 and 2 for Zn^{2+} and Sr^{2+} measurements, respectively. Each solution condition is labeled (e.g., Zn-1) for ease of reference. For the Sr^{2+} solutions, pH was adjusted with NaOH. For the Zn^{2+} solutions, pH was controlled by the addition of HTr (where Tr^- is trifluoromethanesulfonate, a synthetic, noncomplexing, monovalent anion) and buffered by the addition of tris(hydroxymethyl)aminomethane (Tris).

Ionic strength was controlled in both Zn^{2+} and Sr^{2+} measurements by the addition of NaCl. For each ion, measurements were carried out at [NaCl] = 0, 10^{-2}, 10^{-1}, and 1 m, respectively. The dominant solution species under these conditions are Zn^{2+} and Sr^{2+}, respectively, as shown in Fig. 3. Additional measurements were made to check the sensitivity of the condensed-layer ion height to the divalent ion concentration, pH, and background electrolyte. For instance, solutions Zn-11, Zn-12, and Zn-13 had $[Zn^{2+}] = 10^{-6}$ m and pH 10, and solution Zn-8 had $[Zn^{2+}] = 10^{-4}$ m and pH 4.3. Although NaCl was normally used as the background electrolyte, solutions Zn-6, Zn-7, Zn-8, Sr-7, Sr-8, and Sr-9 contained Br^- instead of Cl^- as anion; solution Zn-4 had [NaTr] = 10^{-1} m; and solutions Zn-9, Zn-10, and Zn-11 had [RbCl] = 10^{-1} m. For most solution compositions, measurements were repeated at least once to test stability and reproducibility of the height of the adsorbed divalent ion.

Changes in ionic strength were arranged so that the background electrolyte was varied from low to high concentrations. After measurement of each specific EDL ion, the sample surface was rinsed several times with dilute HCl (10^{-3} m) and then several times with deionized water. A fluorescence spectrum was taken after rinsing to ensure that no divalent ions remained in the sample cell when subsequent adsorption measurements began.

The stability of the sample cell and surface composition were monitored by X-ray fluorescence during the measurements. Ti_$K\alpha$ fluorescence from the substrate rutile crystal, with a characteristic energy of 4.5 keV, is strongly attenuated by the solution and Kapton window at the experimental takeoff angle of ∼6°. Consequently, the Ti fluorescence signal is directly sensitive to the thickness of the aqueous layer because of linear attenuation. Constancy of the Ti signal during each experiment implies that the aqueous-layer thickness does not change over the period of the measurement. The $K\alpha$ fluorescence of

Table 1
Solution conditions for Zn^{2+} measurements (concentration, pH, and ionic strength S), with calculated Debye length Λ of the EDL diffuse-layer, measured coherent position P_{110}, derived ion height δ_{110}, coherent fraction f_{110}, total coverage Θ_{tot}, derived coherent coverage Θ_{coh}, and statistical uncertainty (in parentheses) for each single measurement

Solution	Concentration (m)				pH	S (m)	Λ (Å)	P_{110}	δ_{110} (Å)	f_{110}	Θ_{tot} (ML)	Θ_{coh} (ML)
	$[Zn^{2+}]$	$[Na^+]$	$[Cl^-]$	$[Tr^-]$								
Zn-1	10^{-5}	0	0	2×10^{-5}	8	3.1×10^{-5}	547	0.91 (1)	2.96 (3)	0.63 (3)	0.35 (5)	0.24 (5)
Zn-2	10^{-5}	10^{-2}	10^{-2}	2×10^{-5}	8	10^{-2}	30	0.90 (1)	2.93 (3)	0.61 (2)	0.60 (5)	0.41 (5)
Zn-3	10^{-5}	10^{-1}	10^{-1}	2×10^{-5}	8	10^{-1}	9.6	0.91 (1)	2.96 (3)	0.72 (3)	0.20 (5)	0.16 (5)
Zn-4	10^{-5}	10^{-1}	0	10^{-1}	8	10^{-1}	9.6	0.91 (1)	2.96 (3)	0.72 (2)	0.40 (5)	0.32 (5)
Zn-5	10^{-5}	1	1	2×10^{-5}	8	1	3.0	0.93 (1)	3.02 (3)	0.60 (2)	0.45 (5)	0.30 (5)
Zn-6	10^{-5}	10^{-4}	10^{-4} Br^-	2×10^{-5}	8	1.3×10^{-4}	266	0.93 (1)	3.02 (3)	0.72 (4)	0.50 (5)	0.40 (5)
Zn-7	10^{-5}	5×10^{-4}	5×10^{-4} Br^-	2×10^{-5}	8	5.3×10^{-4}	132	0.92 (1)	2.99 (3)	0.70 (2)	0.50 (5)	0.39 (5)
Zn-8	10^{-4}	5×10^{-4}	5×10^{-4} Br^-	2×10^{-4}	4.3	8×10^{-4}	107	–	–	–	0.20 (5)	–
Zn-9	10^{-5}	10^{-1} Rb^+	10^{-1}	2×10^{-5}	7.9	10^{-1}	9.6	0.92 (1)	2.99 (3)	0.68 (1)	0.60 (5)	0.46 (5)
Zn-10	10^{-5}	10^{-1} Rb^+	10^{-1}	2×10^{-5}	7.9	10^{-1}	9.6	0.94 (1)	3.06 (3)	0.65 (1)	0.60 (5)	0.43 (5)
Zn-11	10^{-6}	10^{-1} Rb^+	10^{-1}	2×10^{-6}	10	10^{-1}	9.6	0.91 (1)	2.96 (3)	0.73 (1)	0.60 (5)	0.49 (5)
Zn-12	10^{-6}	0	0	2×10^{-6}	10	1.02×10^{-4}	302	0.90 (1)	2.93 (3)	0.56 (1)	0.50 (5)	0.31 (5)
Zn-13	10^{-6}	0	0	2×10^{-6}	10	1.02×10^{-4}	302	0.89 (1)	2.89 (3)	0.65 (2)	0.50 (5)	0.37 (5)
Zn-14	10^{-5}	0	0	2×10^{-5}	7.9	3.08×10^{-5}	549	0.92 (1)	2.99 (3)	0.57 (2)	0.55 (5)	0.36 (5)
Zn-15	10^{-5}	0	0	2×10^{-5}	7.9	3.08×10^{-5}	549	0.91 (1)	2.96 (3)	0.37 (2)	0.30 (5)	0.12 (5)
Zn-16	10^{-5}	0	0	2×10^{-5}	8	3.1×10^{-5}	547	0.97 (1)	3.15 (3)	0.52 (2)	0.50 (5)	0.29 (5)
Zn-17	10^{-5}	0	0	2×10^{-5}	8	3.1×10^{-5}	547	0.96 (1)	3.12 (3)	0.46 (1)	0.50 (5)	0.26 (5)
Zn-18	10^{-5}	10^{-1}	10^{-1}	2×10^{-5}	8	10^{-1}	9.6	0.90 (1)	2.93 (3)	0.64 (3)	0.20 (5)	0.14 (5)
Zn-19	10^{-5}	0	0	2×10^{-5}	8	3.1×10^{-5}	547	0.88 (1)	2.86 (3)	0.70 (3)	0.30 (5)	0.23 (5)

Table 2
Solution conditions for Sr^{2+} measurements (concentration, pH, and ionic strength S), with calculated Debye length Λ of the EDL diffuse layer, measured coherent position P_{110}, derived ion height δ_{110}, coherent fraction f_{110}, total coverage Θ_{tot}, derived coherent coverage Θ_{coh}, and statistical uncertainty (in parentheses) for each single measurement

Solution	Concentration (m)				pH	S (m)	Λ (Å)	P_{110}	δ_{110} (Å)	f_{110}	Θ_{tot} (ML)	Θ_{coh} (ML)
	$[Sr^{2+}]$	$[Na^{+}]$	$[Cl^{-}]$	$[OH^{-}]$								
Sr-1	10^{-4}	5×10^{-4}	2×10^{-4}	5×10^{-4}	10.7	8×10^{-4}	107	0.91 (1)	2.96 (3)	0.39 (2)	0.85 (5)	0.33 (5)
Sr-2	10^{-4}	5×10^{-4}	2×10^{-4}	5×10^{-4}	10.7	8×10^{-4}	107	0.91 (1)	2.96 (3)	0.62 (2)	0.50 (5)	0.31 (5)
Sr-3	10^{-4}	10^{-2}	10^{-2}	5×10^{-4}	10.7	10^{-2}	30	0.92 (1)	2.99 (3)	0.59 (2)	0.60 (5)	0.35 (5)
Sr-4	10^{-4}	10^{-1}	10^{-1}	5×10^{-4}	10.7	10^{-1}	9.6	0.91 (1)	2.96 (3)	0.65 (2)	0.40 (5)	0.26 (5)
Sr-5	10^{-4}	1	1	5×10^{-4}	10.7	1	3.0	0.93 (1)	3.02 (3)	0.74 (2)	0.30 (5)	0.22 (5)
Sr-6	10^{-4}	1	1	5×10^{-4}	10.7	1	3.0	0.91 (1)	2.96 (3)	0.74 (2)	0.30 (5)	0.22 (5)
Sr-7	10^{-4}	8×10^{-4}	5×10^{-4} Br^{-}	5×10^{-4}	10.7	1.1×10^{-3}	92	0.93 (1)	3.02 (3)	0.66 (2)	0.50 (5)	0.33 (5)
Sr-8	10^{-4}	9.7×10^{-3}	9.4×10^{-3} Br^{-}	5×10^{-4}	10.7	10^{-2}	30	0.91 (1)	2.96 (3)	0.57 (1)	0.70 (5)	0.40 (5)
Sr-9	10^{-4}	9.7×10^{-3}	9.4×10^{-3} Br^{-}	5×10^{-4}	10.7	10^{-2}	30	0.91 (1)	2.96 (3)	0.60 (1)	0.70 (5)	0.42 (5)
Sr-10	10^{-4}	5×10^{-4}	2×10^{-4}	5×10^{-4}	10.7	8×10^{-4}	108	0.92 (1)	2.99 (3)	0.54 (4)	0.30 (5)	0.16 (5)
Sr-11	10^{-4}	5×10^{-4}	2×10^{-4}	5×10^{-4}	10.7	8×10^{-4}	108	0.90 (2)	2.93 (7)	0.54 (5)	0.40 (5)	0.22 (5)
Sr-12	10^{-4}	5×10^{-4}	2×10^{-4}	5×10^{-4}	10.7	8×10^{-4}	108	0.91 (1)	2.96 (3)	0.51 (2)	0.60 (5)	0.31 (5)
Sr-13	10^{-4}	5×10^{-4}	2×10^{-4}	5×10^{-4}	10.7	8×10^{-4}	108	0.93 (1)	3.02 (3)	0.56 (1)	0.70 (5)	0.39 (5)
Sr-14	10^{-4}	5×10^{-4}	2×10^{-4}	5×10^{-4}	10.7	8×10^{-4}	108	0.93 (1)	3.02 (3)	0.53 (1)	0.80 (5)	0.42 (5)
Sr-15	10^{-4}	5×10^{-4}	2×10^{-4}	5×10^{-4}	10.7	8×10^{-4}	108	0.95 (1)	3.09 (3)	0.55 (1)	0.80 (5)	0.44 (5)

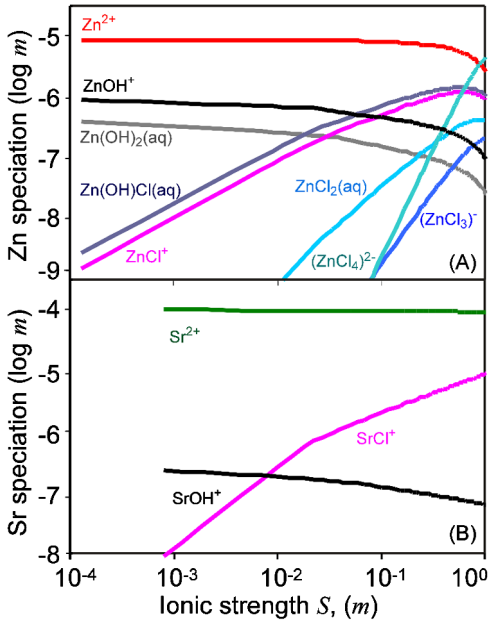

Fig. 3. Speciation calculation for (A) pH 8, $[Zn^{2+}] = 10^{-5}$ m, ionic strength $S = 10^{-4}$–1 m; (B) pH 10.7, $[Sr^{2+}] = 10^{-4}$ m, ionic strength $S = 10^{-3}$–1 m. The ionic strength was adjusted by addition of NaCl. The calculations were performed without equilibration of the solution with atmospheric CO_2.

EDL ions (e.g., Sr^{2+}), on the other hand, is determined by the total coverage of ions, including ions adsorbed at the interface and in the bulk solution, with the latter contribution expected to be proportional to the solution thickness at a given concentration. This provides information about EDL stability, the degree to which ion coverages have equilibrated, and any perturbation induced by the X-ray beam.

Absolute ion coverages were obtained by comparison to measurements of calibrated ion-implanted standards. The absolute total coverage of Zn^{2+} was calibrated with a Ga-implanted silicon wafer (with corrections for differences in atomic cross section, fluorescence yield ratio, attenuation through the water layer, and detector efficiency at the specific energy). The Sr^{2+} coverage was calibrated with a Sr-implanted silicon wafer. For an expected solution layer ∼2 μm thick, the equivalent coverage of ions in the bulk solution would be no more than $1.2 \times 10^{13}/cm^2$, or ∼0.02 ML. This is a much smaller value than the expected or measured ion coverage in the EDL, which is normally >0.2 ML and typically ∼0.5 ML for divalent ions (Tables 1 and 2). This result suggests that the signal from the bulk solution ions is negligible in our measurements. Thus, the XSW measurements reflect the intrinsic distributions of the EDL ions. The bulk solution thickness in the sample cell is substantially greater than the Debye length, Λ, which is <550 Å for all solution conditions probed here. Thus, these XSW measurements reflect the EDL distribution at a free surface–solution interface, with no complications associated with overlapping diffuse layers.

3. Results and discussion

3.1. Cation adsorption: Ion height vs ionic strength

For the specifically adsorbed ions Sr^{2+} and Zn^{2+}, the effect of background electrolyte concentration on the adsorbed cation heights was explored first. The XSW data in Fig. 4 show, for solutions Zn-1 through Zn-5 described in Table 1, the measured rutile TiO_2 (110) reflectivity $R(\theta)$ and Zn^{2+} fluorescence signals $Y(\theta)$ as a function of incident angle $\theta - \theta_b$ (θ_b is the Bragg angle), with the best fit to the data using Eq. (1). Similar data for Sr^{2+} solutions Sr-2 through Sr-5 are plotted in Fig. 5. The coherently averaged Stern layer ion height above the surface Ti–O plane δ_{110} is used in place of P_{110} for simplicity. Here $\delta_{110} = P_{110}d_{110}$, with $d_{110} = 3.25$ Å the d-spacing of the rutile (110) reflection.

The variation of the Stern-layer height (δ_{110}) as a function of the solution ionic strength (S) is summarized in Fig. 6. These

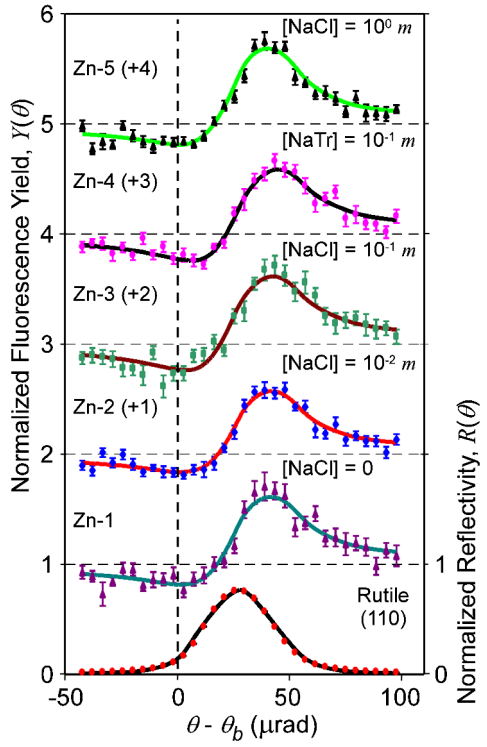

Fig. 4. XSW measurements of Zn^{2+} ion heights at the TiO_2 (110)–aqueous interface as a function of ionic strength S. The normalized TiO_2 (110) reflectivity curve is shown at the bottom. Normalized fluorescence curves for Zn-2 through Zn-5 are vertically offset as indicated. For all solutions, $[Zn^{2+}] = 10^{-5}$ m at pH 8. The electrolyte medium was NaCl in all but Zn-4, where 0.1 m NaTr was used. See Table 1 for more details.

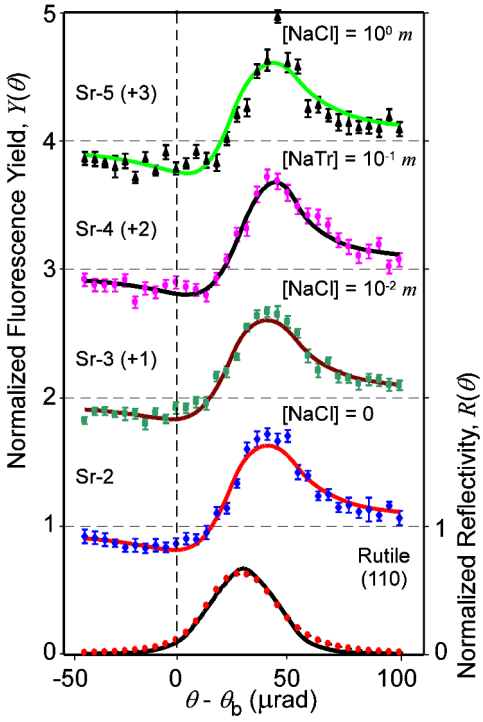

Fig. 5. XSW measurements of Sr^{2+} ion heights at the TiO_2 (110)–aqueous interface as a function of ionic strength S. The normalized TiO_2 (110) reflectivity curve is shown at the bottom. Normalized fluorescence curves for Sr-3 through Sr-5 are vertically offset as indicated. All solutions contained $[Sr^{2+}] = 10^{-4}$ m at pH 10.7. The electrolyte medium was NaCl in all but Sr-4, where 0.1 m NaTr was used. See Table 2 for detailed information about the solutions and results.

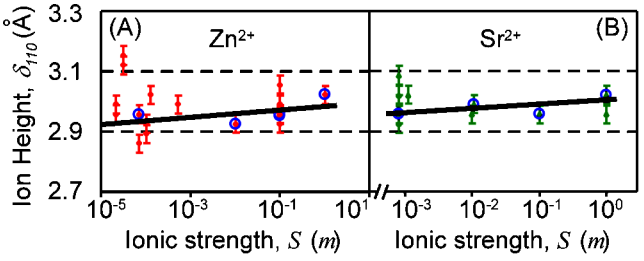

Fig. 6. Coherently adsorbed ion heights δ_{110} as a function of ionic strength S for (A) Zn^{2+} and (B) Sr^{2+}. The lines are fits to the data points shown as open circles, which indicate consecutive measurements made by varying only the background electrolyte concentration, with the functional form $\delta_{110} = k \log_{10}(S) + \delta^0_{110}$. For Sr^{2+}, $k = 0.014 \pm 0.009$ and $\delta^0_{110} = 3.00 \pm 0.03$ Å; for Zn^{2+}, $k = 0.012 \pm 0.014$ and $\delta^0_{110} = 2.98 \pm 0.03$ Å.

data scatter around 3.0 (±0.1) Å and show no significant trend as a function of ionic strength. Specifically, for the measurements Zn-1 through Zn-5 and Sr-2 through Sr-5, which were performed under comparable conditions and are highlighted with circles in Fig. 6, the Stern-layer heights were fitted to a functional form, $\delta_{110} = k \log(S) + \delta^0_{110}$. The best fits were $k = 0.014 \pm 0.009$ and $\delta^0_{110} = 3.00 \pm 0.03$ Å for Sr^{2+} and $k = 0.012 \pm 0.014$ and $\delta^0_{110} = 2.98 \pm 0.03$ Å for Zn^{2+}, where the estimated errors were derived solely from the statistical errors of the individual measurements. The data imply that the Stern-layer heights for adsorbed Zn^{2+} and Sr^{2+} change by only $\sim 0.03 \pm 0.06$ and $\sim 0.06 \pm 0.06$ Å, respectively, while the ionic strength varies over more than 3 orders of magnitude. Given that the statistical uncertainty of an individual measurement is about ±0.03 Å (and the systematic error may be as large as ±0.1 Å), Stern-layer heights for Zn^{2+} and Sr^{2+} show no significant changes in these measurements.

Comparison of the measured coherent positions and coherent fractions at the rutile (110)–aqueous interface with the simulation results based on the GC and GCS ion distribution models (see Appendix A for detail) indicated the following: (1) The GCS model offers a reasonable explanation for the measured coherent fractions and positions at different solution conditions, while the GC model does not. In other words, the divalent ions form a condensed layer with a well-defined position. (2) The divalent ions reside predominantly in the condensed layer, and balance almost all of the surface charge. In such a situation, δ_{110} indicates the Stern-layer height.

3.2. *Cation adsorption: Absolute ion coverages*

The EDL ions balance the surface charge and lead to overall electrical neutrality across the interfacial region. Therefore, the surface charge density, the total number of adsorbed counterions, and the ion distribution should be constant for a given solution condition. Ions may be adsorbed as "inner-sphere" species in direct contact with the surface oxygens or as "outer-sphere" species with their first hydration shells intact [2]. In either case, these ions would be assigned to a Stern layer, and

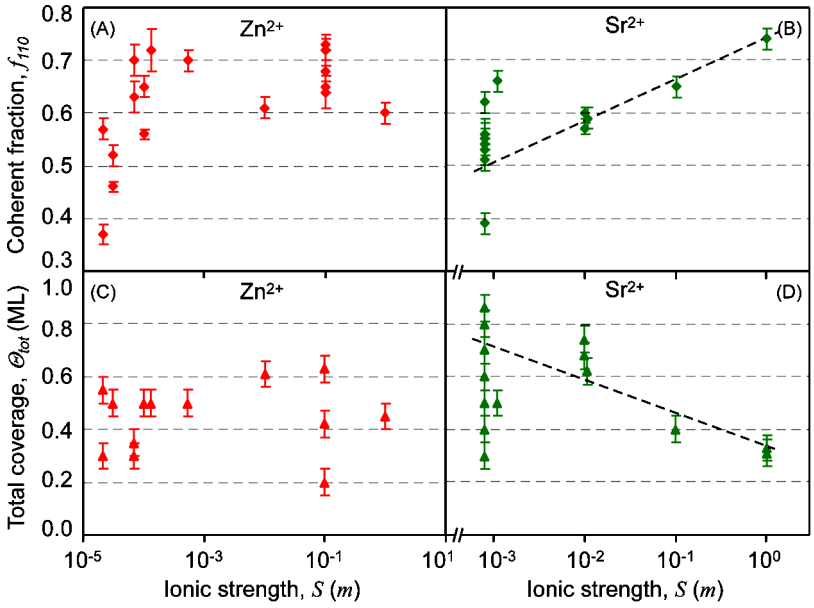

Fig. 7. Measured coherent fraction f_{110} and total ion coverage Θ_{tot} as a function of ionic strength S for Zn^{2+} in (A) and (C) and Sr^{2+} in (B) and (D), respectively. The lines in (B) and (D) are guides for the eye only, suggesting the possible sensitivity of Sr^{2+} ion distribution at $S > 10^{-2}$ m that would be expected if background electrolyte ions were exchanged for Sr^{2+} in the diffuse layer.

the height of this layer above the surface would be related to the bare ionic radius or the hydrated radius, respectively [10,31]. These Stern-layer ions coexist with background electrolyte ions in the diffuse layer, which balances any residual surface charge and decays exponentially to the bulk-solution composition. Such a model was applied previously in SCMs with strictly inner-sphere Stern-layer binding of all cations, along with the Gouy–Chapman approximation of the diffuse-layer ion distribution [31]. We argued in that case that multivalent and monovalent ions compete directly for sorption at specific sites within the Stern layer(s), as well as in the diffuse layer, with monovalent ions being weaker adsorbates. The relative strengths of ions adsorbed at the rutile (110) surface can be probed by looking for changes in the multivalent cation distribution as a function of ionic strength (i.e., monovalent cation concentration) and other solution variables revealed by XSW measurements. Specifically, the displacement of diffuse-layer multivalent ions with background electrolyte ions should result in a decrease of the diffuse-layer multivalent ion coverage, Θ_D, which would further lead to an increase in the coherent fraction, f_H, according to Eqs. (4) and (6). Alternatively, displacement of multivalent ions in the Stern layer by competing background electrolyte ions would decrease the Stern layer multivalent ion coverage, Θ_C, and may lead to a decrease in the coherent fraction. In both scenarios, the total EDL ion coverage would decrease.

The coherent fractions, f_{110}, and the total coverages, Θ_{tot}, of the specifically adsorbed divalent ions are summarized in Fig. 7. The Zn^{2+} data show no significant systematic trends for either f_{110} or Θ_{tot} as a function of ionic strength. Instead, the data appear to vary randomly from one measurement to the next. The Sr^{2+} data appear to show a trend of increasing f_{110} and decreasing Θ_{tot} with increasing ionic strength, as would be expected if the specifically adsorbed Sr^{2+} ions coexisted with a diffuse-ion distribution. However, the data at the lowest ionic strengths are sufficiently variable to prevent us reaching a definitive conclusion.

To reveal the intrinsic EDL ion distribution, we focus on the behavior of the Stern-layer ions. The Stern-layer ion coverage, Θ_C, can be derived from the product of the ordered fraction, C, and the total coverage, Θ_{tot}, as $\Theta_C = C\Theta_{\text{tot}}$. Although it is not directly measurable, C is well approximated by f_H/a_H, as described earlier (when $D_H \approx 1$). Consequently, we use the coherent coverage, $\Theta_{\text{coh}} = f_H\Theta_{\text{tot}}/a_H$, as an approximation for Θ_C. For Sr^{2+}, unique adsorption site leads to $a_{110} = 1$; therefore, $\Theta_{\text{coh}} = f_{110}\Theta_{\text{tot}}$. For Zn^{2+}, if the geometry factor does not depend upon ionic strength, so that $a_{110} = 0.9$, we have $\Theta_{\text{coh}} = f_{110}\Theta_{\text{tot}}/0.9$. The systematic variation of condensed-layer ion height with coherent coverage is shown in Figs. 8A and 8B. The Stern-layer heights are found to be $\delta_{110} = 3.00$ (± 0.10) Å for both Sr^{2+} and Zn^{2+} ions, showing no significant trend as a function of coherent coverage.

Although the measured total EDL coverages were highly variable, plots of Θ_{coh} as a function of Θ_{tot} immediately revealed a strong correlation for both Sr^{2+} and Zn^{2+}, as shown for all XSW measurements using the rutile (110) Bragg reflection (Figs. 8C and 8D). Here the uncertainties in both total and coherent coverages are estimated to be 0.05 ML. For both data sets, Θ_{coh} increases linearly with increasing Θ_{tot}. The data can be fitted to a functional form $\Theta_{\text{coh}} = k\Theta_{\text{tot}}$. For Zn^{2+}, $k = 0.70 \pm 0.02$; for Sr^{2+}, $k = 0.55 \pm 0.02$. Considering that Θ_{coh} is defined as $\Theta_{\text{coh}} = f_H\Theta_{\text{tot}}/a_H$, the slope, $k = f_{110}/a_{110} \approx C$, is the "ordered fraction" out of all ions. A constant k value for an adsorbate under different solution conditions means that the fraction of EDL ions in the Stern layer is constant, which implies no change in the overall EDL structure. The variability of the total coverage, therefore, is not intrinsic to the EDL but is an extrinsic effect. For instance,

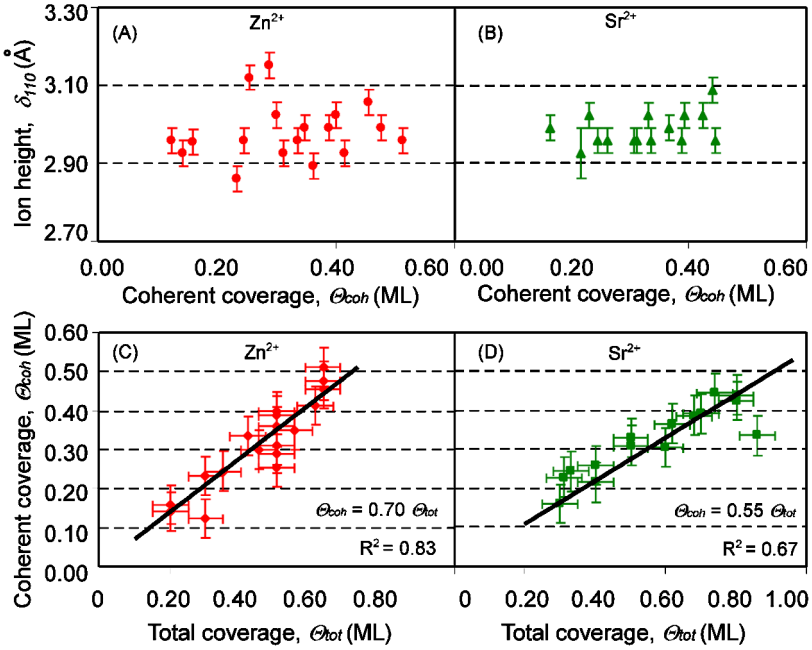

Fig. 8. Adsorbed-ion height δ_{110} as a function of coherent coverage Θ_{coh} for (A) Zn^{2+} and (B) Sr^{2+}. Also shown is the coherent coverage Θ_{coh} as a function of total coverage Θ_{tot} for (C) Zn^{2+} and (D) Sr^{2+}. Lines in (C) and (D) are fits of the data to the functional form $\Theta_{\text{coh}} = k\Theta_{\text{tot}}$, with $k(Zn^{2+}) = 0.70 \pm 0.02$ and $k(Sr^{2+}) = 0.55 \pm 0.02$.

a dirty or defective patch of surface might prevent adsorption of ions and reduce the eventual total coverage. For ions that do become adsorbed to the surface, the EDL structure is the same under our experiment conditions. The slightly lower k value for Sr^{2+} than for Zn^{2+} might suggest a different EDL profile, with a higher partitioning of ions in the diffuse layer for Sr^{2+} than for Zn^{2+}. Unlike Zn^{2+}, the Sr^{2+} data can be fitted better with the functional form $\Theta_{\text{coh}} = k\Theta_{\text{tot}} + b$. This suggests a possible change in EDL profile with ionic strength (specifically, the partitioning of ions between condensed and diffuse layers), although the effect is very subtle, especially considering the uncertainties of the ion coverage measurements. This effect is consistent with the weak variation in Sr^{2+} Stern-layer coverage and coherent fraction summarized in Fig. 7.

For all data with various ionic strengths, the maximum coherent coverage observed was about 0.5 ML for Zn^{2+} and 0.45 ML for Sr^{2+}. In a few cases, the total coverage was substantially higher (e.g., >1 ML) after extended exposure of the sample (∼2 days) to undulator X-ray beams. Even under these circumstances, the coherent coverage never exceeded the maximum values shown in Fig. 8. We believe that this abnormally high total coverage is not intrinsic to EDL. Instead, it appears to arise from ions elsewhere in the in situ cell, for example, on the Kapton window or associated with a preexisting patch of adventitious carbon adsorbed to the rutile surface. Therefore, we conclude that the maximum coherent coverage indicates the saturated Stern-layer coverage for an adsorbate on a perfect rutile (110) crystal surface. If additional ions were incorporated into the condensed layer, we would find either a higher coherent coverage or a different coherent position because of changes in the adsorption sites, yet this was not observed.

In summary, the absence of any sensitivity of the Zn^{2+} coherent position and coherent fraction to ionic strength suggests that few Zn^{2+} ions occur in the diffuse double layer. The absence of variation in coherent coverage and coherent fraction as a function of ionic strength suggests that competition from monovalent ions was negligible under all of our experimental conditions. In comparison, a weak variation in Sr^{2+} coherent coverage and coherent fraction might exist at elevated ionic strength, suggesting displacement of the diffuse-layer ions by background electrolyte ions. At the highest background electrolyte concentrations, the ratios of Na^+ to Sr^{2+} and Zn^{2+} ions in the solution are 10^4 and 10^5, respectively. Therefore, the adsorption strength of Na^+ at the rutile (110)–aqueous interface is lower by at least 4 or 5 orders of magnitudes than that of Sr^{2+} and Zn^{2+}.

The data in Fig. 8 provide some insight into the variability of the data in Fig. 7. The total coverage might not be simply related to the intrinsic EDL structure, but it might be affected by extrinsic factors such as crystal surface quality. Although we used the highest quality samples available, the variability in total coverage suggests that our samples were not perfectly homogeneous. Consequently, no simple correlations can be made between total coverage and ionic strength.

The saturated coherent coverages for Sr^{2+} and Zn^{2+} ions, as discussed above, appear to be a good approximation of the actual intrinsic EDL ion coverages under these conditions. Both Sr^{2+} and Zn^{2+} ions are adsorbed at rutile (110) surface primarily as inner-sphere complexes; i.e., they lose some of their hydration shell water molecules to bond to the surface oxygen site(s). These ions most likely retain part of the hydration shell upon adsorption which could limit their coverages. The maximum inner-sphere adsorbed ion coverage can be estimated by

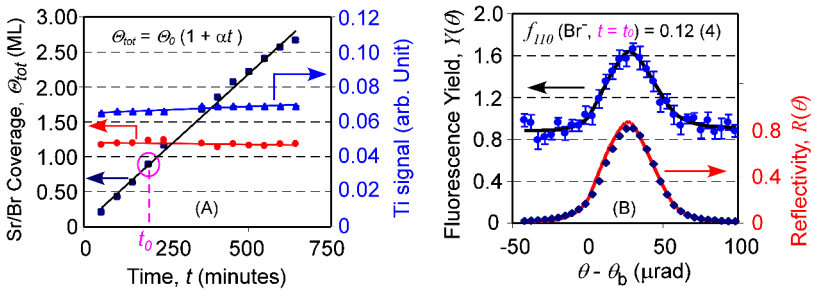

Fig. 9. (A) Total fluorescence signals of Sr^{2+}, Br^-, and Ti in the system as a function of time, with the fit to the functional form of $\Theta_{tot} = \Theta_0(1 + \alpha t)$. These data give $\alpha(Sr^{2+}) = -5 \times 10^{-5}$, $\alpha(Ti) = 1 \times 10^{-4}$, and $\alpha(Br^-) = 0.11$. (B) The measured Br^- XSW data at the TiO_2 (110) Bragg peak at time $t = t_0$, marked with a circle in (A).

assuming that the lateral size of the adsorbed hydrated ion is similar to that found in solution, which is ∼6 Å for Sr^{2+} and Zn^{2+} [47]. This suggests a maximum coverage of ∼0.5 ML (∼1 ion per 40 $Å^2$), which agrees with what we observed experimentally. The results imply that the surface charges of the rutile (110) surface may be fully compensated by the adsorbed ions, consistent with the observation that no significant contribution from diffuse-layer ions was observed under our experiment conditions. This would suggest that any additional increase in surface charge might result in the development of outer-sphere complexes or diffuse layer.

3.3. Anion adsorption

A more subtle issue concerns the role of anions in controlling or influencing cation adsorption. Anions might form ternary sorption complexes with multivalent cations at the interface [48–51], leading, for example, to the adsorption of $ZnCl^+$ or $ZnCl_2^0$ instead of Zn^{2+} at the rutile–water interface. We explored this effect in two ways. First, we looked for changes in cation height for various background anions (Cl^-, Br^-, and Tr^-) and cations (Na^+ and Rb^+). The absence of the effect on the height of the specifically adsorbed divalent cations (Fig. 6, Tables 1 and 2) demonstrates the insensitivity of Sr^{2+} and Zn^{2+} ion heights to the presence of Cl^-, Br^-, and Tr^- anions. Because the tendencies of these anions to form ion pairs with Sr^{2+} and Zn^{2+} differ strongly, this observation suggests that these anions do not form ternary adsorption complexes with Sr^{2+} or Zn^{2+} at the rutile (110)–aqueous interface.

To probe the role of anions in the EDL structure more directly, we used Br^-, an anion whose $K\alpha$ fluorescence can penetrate the water film and can therefore be measured directly by XSW. Unlike the measurements described above in which cation adsorption was stable during X-ray exposure in XSW measurements, the Br^- fluorescence signal had a substantial X-ray-induced time dependence. Representative measurements of a solution with pH 10.7, $[SrBr_2] = 10^{-4}$ m, and $[NaBr] = 3 \times 10^{-4}$ m are shown in Fig. 9A, in which the off-Bragg X-ray fluorescence signals for Sr^{2+}, Br^-, and bulk Ti are plotted as a function of time. The Ti signal provides a direct measure of the stability of the solution thickness. The small positive and negative slopes for Ti and Sr^{2+}, respectively, can be explained by a slight (<10%) reduction in solution thickness during these measurements. Both coherent positions and coherent fractions of Sr^{2+} were unchanged over these measurements, indicating that the EDL cation distribution was stable. The change in Br^- signal with time, however, was large, and the Br^- coverage eventually exceeded that of the adsorbed Sr^{2+}. Extrapolating this time variation to zero (when the sample was first exposed to the X-ray beam) gave an intrinsic Br^- coverage of ∼0.04 ML, which is approximately the expected value for Br^- ions in the bulk solution (implying that Br^- is not significantly associated with the rutile surface in the absence of the X-ray beam). Measurements of separate spots on the same surface showed similar Br^- signal levels, suggesting that these changes were not localized to the specific X-ray footprint. After flushing of the cell with fresh solution, the Br^- signal returned to its time-zero level and grew again with the same linear trend. The cause of this increasing Br^- signal is not understood at present, but it appears to be due to an X-ray-related perturbation (e.g., charge buildup on the Kapton window). Once the Br^- fluorescence signal was strong enough to be measured, XSW data showed no significant Br^- ordering at the interface, as indicated by negligible Br^- coherent fractions (Fig. 9B).

The observations of negligible Br^- coherent fractions and an initial intrinsic Br^- coverage that is consistent with the bulk Br^- concentration suggest that no significant Br^- coadsorption with Sr^{2+} occurs at the rutile (110) interface under our experiment conditions. The time dependence of the Br^- signal was unlike that of the other ions we have studied with XSW (Sr^{2+}, Zn^{2+}, and Y^{3+}), for which the fluorescence signal was typically stable over extended periods [31].

3.4. Quantitative comparison to surface complexation model predictions

We previously showed that the MUSIC model is capable of incorporating the detailed cation height and adsorption site measured by XSW and CTR with traditional macroscopic information (e.g., proton desorption enthalpies and ion adsorption behavior) [31]. The MUSIC model can also use this information to make direct predictions of condensed-layer ion coverage and partitioning of the cation between condensed and diffuse layers as a function of solution conditions. The data described above therefore present an additional way to directly test the predictions of the MUSIC model with experimental XSW results and establish additional connections between molecular-scale structure and macroscopic properties of the EDL.

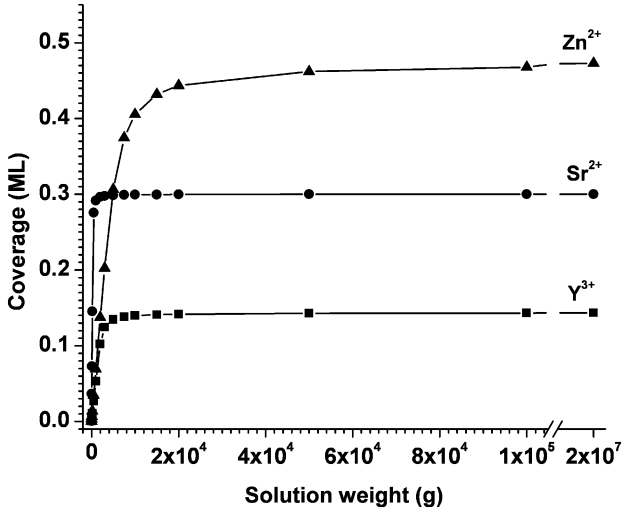

Fig. 10. Simulated coverage (ML) for Zn^{2+} (10^{-5} m, pH 8, $S = 3 \times 10^{-2}$ m), Sr^{2+} (10^{-4} m, pH 10.7, $S = 10^{-3}$ m), and Y^{3+} (10^{-5} m, pH 6.1, $S = 5 \times 10^{-4}$ m) with increasing solution weight (at fixed solid surface area), as predicted by using model parameters fitted to rutile powder titration data presented in Ref. [31]. The X axis contains a break in scale for clarity.

The MUSIC model results were extrapolated from fits to titration data for rutile powders by increasing the solution-to-solid ratio (the solution weight) from values typical of our powder titrations (50:1) to the essentially infinite ratios (20,000,000:1) appropriate for our XSW experiments, while keeping all model parameters constant. These model parameter values and other details concerning our modeling efforts were published previously [31]. Representative results of simulations for Sr^{2+}, Zn^{2+}, and Y^{3+} (Fig. 10) show the expected trend of Langmuir isotherm behavior with increased adsorption of cations as solution-to-solid ratios increase, until a cation-specific plateau is reached as residual solution cation concentrations approach bulk values.

Results from a similar set of simulations over a range of ionic strengths are presented in Fig. 11, together with the measured values. As discussed above, we used the coherent coverage as an estimate of the Stern-layer coverage. Because we are interested in the saturation coverage for a perfect surface, we took the highest coherent coverage at a given ionic strength. This comparison shows that the MUSIC model predictions, in absolute units and with no adjustable parameters, are remarkably close to the saturation coverages derived from the XSW data. The differences between the experimental and the model predictions are typically ∼20%, similar to the statistical error of the XSW measurements. Although the measured data show no clear trend as a function of ionic strength, the slightly decreasing condensed-layer coverage predicted by the MUSIC model is clearly within the range of the experimental observations.

Table 3 compares X-ray measurements and MUSIC model calculations at identical solution conditions for Sr^{2+} and Zn^{2+} ions and includes results for adsorption of Rb^{+} and Y^{3+} to the rutile–water interface. The minimum coherent coverage of Y^{3+} is estimated from our previous XSW imaging study [30], while the coverage for Rb^{+} is estimated from previous CTR measurements [31]. In addition to the Stern-layer ion coverage (Θ_C), Table 3 shows the fraction of total surface charge ($Q_C + Q_D$) compensated for in the Stern layer (Q_C), $Q^* = Q_C/(Q_C + Q_D)$, as predicted by our MUSIC model simulations. This value is a good approximation for the ordered fraction, $C = \Theta_C/(\Theta_C + \Theta_D)$ if the coverage of ions extrin-

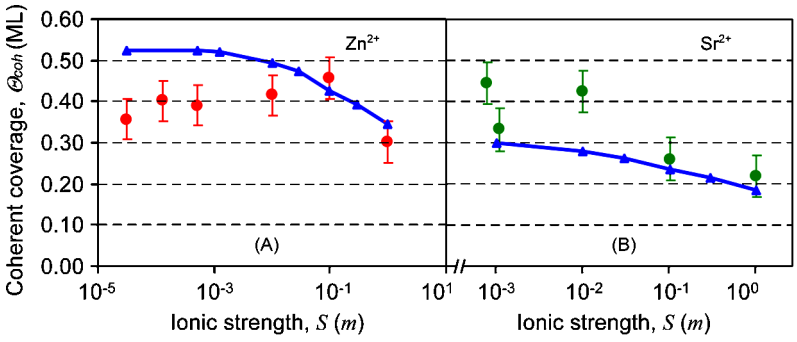

Fig. 11. Coherent coverage (saturated), Θ_{coh}, vs ionic strength, S, for (A) Zn^{2+} and (B) Sr^{2+}. The XSW measurements are shown as points; predictions of the MUSIC model are shown as the line with markers.

Table 3
Stern-layer coverages from XSW and CTR measurements with results predicted by the MUSIC model at the rutile (110)–aqueous interface

Ions	Solution conditions			XSW measurements		MUSIC predictions	
	pH	$[Me^{+}]$ (m)	S (m)	Θ_{coh} (ML)	C	Θ_C (ML)	Q^*
Zn^{2+}	8	10^{-5}	1.3×10^{-3}	∼0.50	0.73	0.52	0.98
Sr^{2+}	10.7	10^{-4}	10^{-3}	∼0.45	0.60	0.30	0.96
Y^{3+}	6.1	10^{-5}	5×10^{-4}	⩾0.1[a]	>0.50	0.14	1.006
Rb^{+}	12	1	1	0.25–0.50[a]	No data	0.20	0.434
	11	10^{-3}	10^{-3}	<0.05	0.05	0.08	0.40

The fraction $Q^* = Q_C/(Q_C + Q_D)$ as predicted by the MUSIC model fits is a good approximation for the ordered fraction $C = f_{110}/a_{110}$.
[a] From Ref. [31].

sic to EDL (Θ_{other}) is negligible. In reality, Θ_{other} could never be zero, and the measured value C is always less than Q^*. The MUSIC model captures the EDL feature that multivalent ions reside mainly in the condensed layer, while monovalent ions are more abundant in the diffuse layer. The MUSIC model predicts that at high Rb^+ concentrations (1 m), significant amount of Rb^+ ions are present in the condensed layer at the rutile (110)–aqueous interface as earlier measurements showed [31]. It also suggests that more Rb^+ ions exist in the diffuse layer than in the condensed layer even at high Rb^+ concentrations, which was not able to be uniquely determined from the measurements.

4. Summary

Our direct measurements of the Stern layer position of divalent ions at the rutile (110)–aqueous interface show for the first time that the position is largely independent of solution conditions, even with changes in ionic strength spanning three orders of magnitude. The presence of other monovalent ions (Cl^-, Br^-, Tr^-, or Rb^+) had negligible effects on the condensed-layer heights. The present results provide direct proof that the GCS model is suitable for describing divalent ions at the rutile (110)–aqueous interface.

The insensitivity of the coherent position and coherent fraction to ionic strength suggests that the proportion of divalent ions either in the diffuse double layer or in the bulk solution is small relative to that in the Stern layer. The implication that the rutile (110) surface charge is primarily compensated by divalent ions under these solution conditions is supported by MUSIC model simulations. Noticeable differences between Zn^{2+} and Sr^{2+} adsorption behaviors imply that Zn^{2+} ions are more strongly bound adsorbates than Sr^{2+} at the rutile (110)–aqueous solution interface. For Zn^{2+} and Sr^{2+}, we found saturated coherent coverages of ∼0.5 and 0.45 ML, respectively. Under our experimental conditions, the adsorption strength of Na^+ or Rb^+ was lower by more than 4 orders of magnitude than that of Sr^{2+} or Zn^{2+}.

The predictions of the Stern-layer ion coverages from the MUSIC model agree well with the measured results in absolute units, providing independent support for the model. Previously, such surface complexation models could only be tested by comparison with macroscopic properties such as proton charge. We have demonstrated that macroscopic models and microscopic structures can be linked directly to provide a powerful method to explore EDL phenomena.

Acknowledgments

These experiments were performed at beamline 12-ID-D (BESSRC-CAT) at the APS and at the beamline X15A at the NSLS. We thank the beamline staff, especially Dr. Zhong Zhong at the NSLS, for help with the experiment setup. The U.S. Department of Energy, Office of Science, Office of Basic Energy Sciences, supported this work through its Chemical Sciences, Geosciences, and Biosciences Division and also supported use of the APS under contract W-31-109-ENG-38.

Appendix A. Direct comparison of EDL models and XSW data

In the simplest EDL model, the GC model (also known as the diffuse-layer model), surface charge is compensated for by a continuous, exponentially varying ion distribution that can be written as [52]

$$\rho(z) = \rho_0 \exp\left[-\frac{z}{\Lambda}\right] + C_0, \quad 0 \leqslant z \leqslant z_{\max}, \tag{A.1}$$

where ρ_0 is the ion concentration at the interface; Λ is the Debye length of the diffuse layer exponential distribution; C_0 is the ion concentration in the bulk solution; and $z_{\max}$ is the solution thickness. The finite ion size and charge repulsion between adsorbates make it reasonable to assume the presence of a thin layer next to the interface with a saturated ion concentration ρ_0 [16]. In addition to the continuous exponential distribution, the GCS model includes a layer of counterions at a well-defined position adjacent to the interface, known as the Stern or condensed layer.

The ion distribution function of the GC model, including the saturation layer, can be written as

$$\rho_{\text{GC}}(z) = \begin{cases} \frac{\Theta_{\text{EDL}}}{2\Delta+\Lambda} & z_0 - \Delta \leqslant z \leqslant z_1, \\ \frac{\Theta_{\text{EDL}}}{2\Delta+\Lambda} \exp\left[-\frac{z-z_1}{\Lambda}\right] + C_0 & z_1 < z \leqslant z_{\max}. \end{cases} \tag{A.2}$$

Similarly, the normalized ion distribution function of the GCS model can be written as

$$\rho_{\text{GCS}}(z) = \begin{cases} x\Theta_{\text{EDL}}\delta(z - z_0) & 0 \leqslant z < z_1, \\ \frac{(1-x)\Theta_{\text{EDL}}}{\Lambda} \exp\left[-\frac{z-z_1}{\Lambda}\right] + C_0 & z_1 \leqslant z \leqslant z_{\max}, \end{cases} \tag{A.3}$$

where Θ_{EDL} is the coverage of the EDL ions, which is related to the surface charge; x ($0 \leqslant x \leqslant 1$) is the partition number of the EDL ions in the condensed layer (that is, the coverages of the condensed-layer and diffuse-layer ions are $\Theta_C = x\Theta_{\text{EDL}}$ and $\Theta_D = (1-x)\Theta_{\text{EDL}}$, respectively); $z_1 = z_0 + \Delta$ is the starting position of the diffuse layer from the interface (the so-called d-plane height); z_0 is the center position of the condensed-layer (the so-called β-plane height); Δ is the distance from the d-plane to the β-plane (for instance, in Ref. [16], $\Delta = 0$); and Λ is the Debye length of the diffuse layer. Here $\exp[-(z_{\max} - z_1)/\Lambda] = 0$ is used, since $z_{\max} \gg z_1$ and $z_{\max} \gg \Lambda$.

The normalized distribution function would simply be $\rho(z)/\Theta_{\text{tot}}$ where the total coverage of ions in the system is

$$\Theta_{\text{tot}} = \int_0^\infty \rho(z)\,\mathrm{d}z = \Theta_{\text{EDL}} + C_0(z_{\max} - z_1). \tag{A.4}$$

Therefore, the fraction of the ions in the EDL is defined as

$$c_{\text{EDL}} = \Theta_{\text{EDL}}/\Theta_{\text{tot}} = 1 - C_0(z_{\max} - z_1)/\Theta_{\text{tot}} = 1 - c_0, \tag{A.5}$$

where $c_0 = C_0(z_{\max} - z_1)/\Theta_{\text{tot}}$.

To account for the expected breadth of the EDL ion positions, two Gaussian functions with different widths were used for convolution with the functions describing the condensed and diffuse parts of the EDL, respectively. Because the GC model

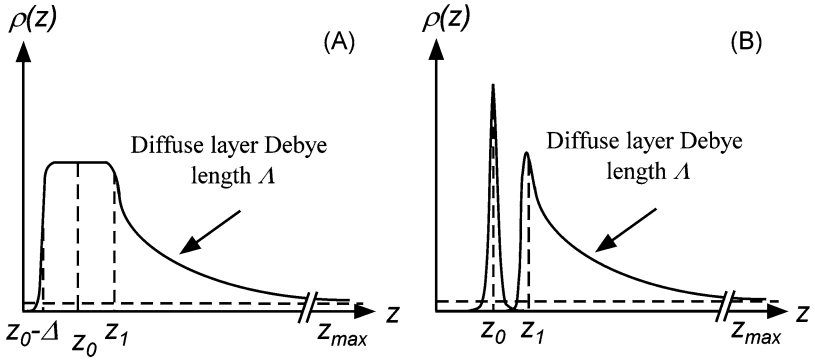

Fig. A.1. Schematic of the EDL ion distribution profile. (A) Gaussian smeared GC model. (B) Gaussian smeared GCS model.

has no condensed layer, only one Gaussian function is used there. Closer to realistic distribution profiles for the GC and GCS models can be achieved this way, as is shown schematically in Figs. A.1A and A.1B, respectively.

For the 1-D ion distribution function, $\rho(z)$, Eq. (2) can be rewritten as

$$f_H \exp[i2\pi P_H] = \mathbf{F}(H) = \int_{-\infty}^{\infty} \rho(z) \exp[iHz]\,\mathrm{d}z. \tag{A.6}$$

The inverse Fourier transforms of the normalized ion distributions are

$$\mathbf{F}_{\mathrm{GC}}(H) = \frac{c_{\mathrm{EDL}} \exp[iHz_0]}{(2\Delta + \Lambda)} \left(\frac{2\sin(H\Delta)}{H} + \frac{\Lambda \exp[iH\Delta]}{(1 - iH\Lambda)} \right) \times \exp\left[-\frac{H^2\sigma_D^2}{2} \right] + \mathbf{F}_{\mathrm{bulk}}(H), \tag{A.7}$$

$$\mathbf{F}_{\mathrm{GCS}}(H) = c_{\mathrm{EDL}} \exp[iHz_0] \left(x \exp\left[-\frac{H^2\sigma_C^2}{2} \right] + \frac{(1-x)\exp[iH\Delta]}{(1 - iH\Lambda)} \exp\left[-\frac{H^2\sigma_D^2}{2} \right] \right) + \mathbf{F}_{\mathrm{bulk}}(H), \tag{A.8}$$

$$\mathbf{F}_{\mathrm{bulk}}(H) = \frac{c_0(\exp[iHz_1] - \exp[iHz_{\max}])}{iHz_{\max}}. \tag{A.9}$$

Here σ_C and σ_D are the Gaussian function widths for condensed and diffuse layers, respectively, and $\mathbf{F}_{\mathrm{bulk}}(H)$ represents the contribution of ions in the bulk solution.

Other potential sources of ions in the system that are not included in the models are those not associated with the rutile (110) surface, for example, adsorption to surface-adsorbed adventitious carbon or the Kapton window. Such other sources of ions are normally randomly or homogeneously distributed over a broad range and would have contributions similar to those of the bulk-solution ions. Therefore, we may consider them as equivalent to bulk-solution ions. For simplicity, hereafter c_0 includes all the ions extrinsic to EDL. The $\mathbf{F}_{\mathrm{bulk}}(H)$ term becomes $\mathbf{F}_{\mathrm{other}}(H)$, or

$$\mathbf{F}_{\mathrm{other}}(H) = \frac{c_0(\exp[-iHz_1] - \exp[-iHz_{\max}])}{iHz_{\max}}. \tag{A.10}$$

Because of the periodicity of the exponential term $\exp[i(Hz \pm 2\pi)] = \exp[iHz]$ and the fact that normally $z_{\max} - z_1 \gg 2\pi/H = d_H$, we can approximate that $\exp[iHz_1] - \exp[iHz_{\max}] = 0$, or $\mathbf{F}_{\mathrm{other}}(H) = 0$. This implies that randomly distributed sources make little if any contribution to the phase of the Fourier transformation (the coherent position, P_H). These sources do, however, reduce the amplitude of the Fourier transformation (the coherent fraction, f_H) by reducing $c_{\mathrm{EDL}} = 1 - c_0$ as c_0 increases for a given EDL system. Therefore, $\mathbf{F}_{\mathrm{other}}(H)$ is not included explicitly below. Instead, its effect is carried into the simulation by varying c_{EDL}. The Fourier transformations of the normalized ion distributions are written as

$$\mathbf{F}_{\mathrm{GC}}(H) = \frac{c_{\mathrm{EDL}} \exp[iHz_0]}{(2\Delta + \Lambda)} \left(\frac{2\sin(H\Delta)}{H} + \frac{\Lambda \exp[iH\Delta]}{(1 - iH\Lambda)} \right) \times \exp\left[-\frac{H^2\sigma_D^2}{2} \right], \tag{A.11}$$

$$\mathbf{F}_{\mathrm{GCS}}(H) = c_{\mathrm{EDL}} \exp[iHz_0] \left(x \exp\left[-\frac{H^2\sigma_C^2}{2} \right] + \frac{(1-x)\exp[iH\Delta]}{(1 - iH\Lambda)} \exp\left[-\frac{H^2\sigma_D^2}{2} \right] \right). \tag{A.12}$$

Combining Eq. (2) with Eq. (A.11) or Eq. (A.12) allows us to calculate the coherent fraction f_H and the coherent position P_H from a specific ion distribution $\rho(z)$ at a given H. For the GCS model (with $x = 1$ and $c_0 = 0$, which means that all the ions are in the condensed layer), we find $\mathbf{F}_{\mathrm{GCS}}(H) = \exp[iHz_0]\exp[-H^2\sigma_C^2/2]$. Consequently, $f_H = |\mathbf{F}_{\mathrm{GCS}}(H)| = \exp[-H^2\sigma_C^2/2] = D_H$, $P_H = Hz_0/2\pi = z_0/d_H$, and $\delta_H = P_H d_H = z_0$ is the condensed-layer height referenced to the bulk lattice planes. The Gaussian term, accounting for factors such as thermal vibration, does not affect the coherent position.

The coherent fraction f_H and coherent position P_H are calculated as a function of the fraction of EDL ions in the condensed layer, x, and the diffuse-layer Debye length, Λ, for both models. The parameters are listed in Table A.1. In all but one of the calculations, the coverage of the ions in the EDL is 10 times that in other sources; that is, $c_{\mathrm{EDL}} = 0.91$, which is the nominal upper limit for ions from the bulk solution under our experimental conditions. $c_{\mathrm{EDL}} = 0.50$ is checked in one calculation for comparison.

We used typical values of $z_0 = 3.0$ Å and $\Delta = 2.0$–3.0 Å in all calculations. The Gaussian distribution widths were set at $\sigma_C = 0.1$ Å, which is the typical vibration amplitude of atoms

Table A.1
Values of parameters used for calculations of coherent fractions and positions with the different EDL models (see text for the meanings of all parameters)

Model	c_{EDL}	Δ (Å)	Λ (Å)	z_0 (Å)	σ_C (Å)	σ_D (Å)
GCS1	0.91	2.0	4			
GCS2	0.91	2.0	24			
GCS3	0.91	2.0	137			
GCS4	0.50	2.0	104	3.0	0.1	1.0
GCS5	0.91	2.5	104			
GC1	0.91	2.0	4			
GC2	0.91	2.0	70			

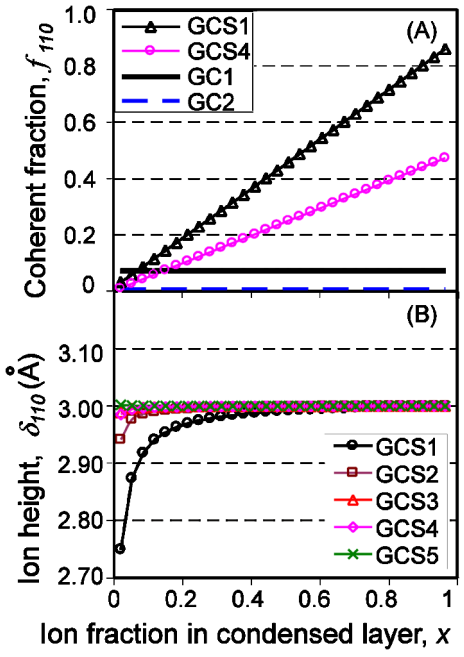

Fig. A.2. Simulated (A) coherent fraction f_{110} and (B) ion height δ_{110} as a function of the fraction of the EDL ions in the condensed layer x for models GC1 and GC2 and GCS1 through GCS5, respectively.

in the bulk rutile crystal (<0.1 Å) [53], and $\sigma_D = 1$ Å, which is a typical value for water molecules near a solid–aqueous interface (∼1 Å) [23]. From the solution ionic strength, the Debye length of the diffuse layer, Λ, was estimated at 3–600 Å. A few representative values were chosen for the simulations. The calculated coherent fractions as a function of the condensed-layer ion partition numbers for both the GC and the GCS models at different Debye lengths are plotted in Figs. A.2A and A.2B.

That the GC model, which consistently predicts coherent fractions close to zero, does not describe the divalent ion distribution at the rutile (110)–aqueous interface properly is apparent from our observation of much higher coherent fractions in all of our measurements. For instance, for Sr^{2+} solution Sr-3 with $[NaCl] = 10^{-2}$ m, the measured coherent fraction $f_H = 0.59$, whereas calculation with the GC model predicts a coherent fraction ∼0 for any value of condensed-layer occupation at the expected condition of $\Lambda \sim 30$ Å.

On the other hand, the GCS model provides a reasonable explanation for the measured coherent fractions. This finding confirms that the divalent ions form a condensed layer with a well-defined position at the rutile (110)–aqueous interface under our experimental conditions. Consequently, we now focus on the GCS model. The calculated coherent fractions for different values of Λ are indistinguishable. If they were plotted in Fig. A.2A, calculations with the GCS2, GCS3, and GCS5 models would yield exactly the same result as that of GCS1. This observation establishes that the coherent fraction is independent of the diffuse-layer Debye length Λ (as expected, since the period of the Bragg XSW field is substantially smaller than the Debye length). Instead, these results establish that the coherent fraction is determined primarily by the partitioning of ions in the condensed layer, x. Similarly, the coherent fraction is largely independent of the other two parameters describing the EDL structure: Δ, the distance between the d-plane and the β-plane, and z_0, the condensed-layer ion height.

In our experiments, the coherent fractions are typically in the range of 0.5 to 0.75. Thus, we can estimate that the fraction of the EDL ions in the condensed layer must be greater than 0.5. Under these circumstances, the calculated coherent position is expected to be independent of x, Δ, c_{EDL}, and Λ, being determined solely by the height of the condensed-layer ions, z_0. The effect of the diffuse layer ion on the coherent position (<0.01 Å) is also well below our sensitivity limit (0.02 Å). Only when the coherent fraction is very low and the Debye length is very short do the coherent positions deviate from the typical value determined by z_0. This scenario is not relevant to the present measurements. Therefore, in the Bragg XSW measurements of divalent ions adsorbed at the rutile (110)–aqueous interface, the coherent fractions and coherent positions do not directly represent the diffuse-layer ion distributions.

For a weakly bound adsorbate such as Rb^+, the diffuse ions are dominant (e.g., $x < 0.1$) under similar conditions (i.e., $[Rb^+] < 10^{-3}$ m). The coherent fraction will be ∼0, as observed in our measurements and predicted by the GC model [31].

According to the calculations above, the coherent fraction is close to the fraction of all ions found in the condensed layer, xc_{EDL}. The ions in the diffuse layer, $(1-x)c_{EDL}$, and other sources, $c_0 = 1 - c_{EDL}$, are indistinguishable by coherent position and coherent fraction in a single measurement. Neither has an effect on the coherent position, adding only to the incoherent fraction of the total ions. However, the diffuse-layer ions balance part of the surface charge. Direct measurement of the surface charge inevitably requires evaluation of the coverages of the diffuse-layer and the condensed-layer ions. Because the measured Bragg XSW parameters do not directly present information about the diffuse-layer ion distribution, we must look at the variation of the coherent fraction as a function of solution parameters.

If incoherent ions occur primarily in the diffuse layer, the total coverage of divalent ions should decrease when the background electrolyte concentration increases significantly because of competition from the background electrolyte. For instance, in the solution where $[Zn^{2+}] = 10^{-5}$ m and $[Na^+] = 1$ m, the diffuse layer will predominantly consist of Na^+ ions that are overwhelmingly abundant in the solution, while the coverage of inner-sphere Zn^{2+} complexes adsorbed in the condensed layer will be unchanged. Therefore, a decrease in the

total Zn^{2+} coverage will be directly related to the partitioning of Zn^{2+} and Na^{+} in the diffuse layer.

With Zn^{2+} displaced from the diffuse layer, the coherent fraction will increase, as predicted in Fig. A.2A. This was not observed, however, with the measured coherent fractions. Figs. 7A and 7C show no systematic trend in either the coverage or the coherent fraction for Zn^{2+} as a function of the solution ionic strength. This observation indicates that the incoherent ions are not primarily from the diffuse layer but from other sources. This observation also implies that the divalent condensed-layer ions compensate for most or all of the surface charges. A weak variation of these parameters is suggested by the Sr^{2+} data (Figs. 7B and 7D), especially at ionic strengths $S > 10^{-2}\,m$, potentially indicating a modest partitioning of ions between the condensed and the diffuse layers.

The discussion above assumes that the condensed-layer ions have a unique height, which is not always the case. For instance, in the XSW triangulation of Sr^{2+} and Zn^{2+} at the rutile (110)–aqueous interface, we found a single Sr^{2+} height but two substantially different Zn^{2+} heights, with the predominant species at a height of 3.16 ± 0.14 Å above the surface Ti–O plane (with >75% of the Stern-layer Zn^{2+}) and the minor species at a height of 2.70 ± 0.25 Å (with <25% of the Stern-layer Zn^{2+}) [31]. In this case, the measured coherent position is affected not only by the height of each of the multiple positions but also by the partitioning of ions between those positions.

Because diffuse-layer divalent ions are known to make a negligible contribution to the measured coherent position, we will ignore them in investigations of the influence of multiple condensed-layer ion heights. For simplicity, we assume that the distributions of ions are a series of δ-functions at different heights, convoluted with a normalized Gaussian distribution. The inverse Fourier transformation of such a distribution would be

$$\begin{aligned}\mathbf{F}_m(H) &= \int_{-\infty}^{+\infty}\left\{\sum_j c_{C\_j}\delta(z - z_{C\_j}) \otimes \frac{1}{\sigma_j\sqrt{2\pi}}\right.\\ &\quad\left.\times \exp\left[-\frac{z^2}{2\sigma_{C\_j}^2}\right]\right\}\exp[iHz]\,\mathrm{d}z\\ &= \sum_j c_{C\_j}\exp[iHz_{C\_j}]\exp\left[-\frac{H^2\sigma_{C\_j}^2}{2}\right]. \qquad \text{(A.13)}\end{aligned}$$

Here c_{C_j} and σ_{C_j} are the partitioning and the Gaussian distribution width of the ions at height z_{C_j}, respectively. If we assume that all condensed-layer ions have the same Gaussian distribution width, $\sigma_{C\_j} = \sigma_C$, the inverse Fourier transformation of the ion distribution with two heights is given as

$$\begin{aligned}\mathbf{F}_m(H) &= \left(c_{C\_1}\exp[iHz_{C\_1}] + c_{C\_2}\exp[iHz_{C\_2}]\right)\\ &\quad\times\exp\left[-\frac{H^2\sigma_C^2}{2}\right], \qquad \text{(A.14)}\end{aligned}$$

instead of

$$\mathbf{F}_s(H) = c_{\mathrm{EDL}}\exp\left[iH\overline{z_C}\right]\exp\left[-\frac{H^2\sigma_C^2}{2}\right], \qquad \text{(A.15)}$$

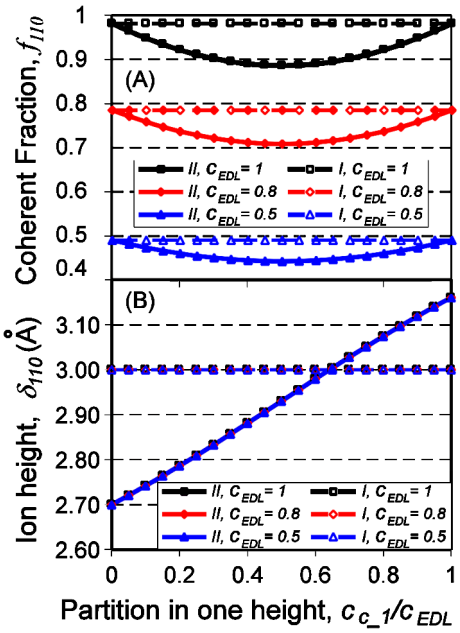

Fig. A.3. Simulated (A) coherent fractions f_{110} and (B) ion height δ_{110} as a function of the fractional occupation of the ions c_{C_1}/c_{EDL} at height $z_{C\_1} = 3.16$ Å, for the one-height (I, dashed lines and open markers) and two-height (II, solid lines and filled markers) models. Parameters used in the simulations (explained in the text): $\overline{z_C} = 3.0$ Å, $\sigma_C = 0.1$ Å, and $c_{\mathrm{EDL}} = 1$, 0.8, and 0.5, respectively. Note that in (B) exactly the same coherent positions were calculated by each model with different c_{EDL} values.

which is the appropriate form for a single ion height distribution, where $c_{\mathrm{EDL}} = c_{C\_1} + c_{C\_2}$ is the total condensed-layer coverage; $\overline{z_C}$ is the weighted average position of the two heights, z_{C_1} and z_{C_2}. That is,

$$\overline{z_C} = \frac{c_{C\_1}z_{C\_1} + c_{C\_2}z_{C\_2}}{c_{C\_1} + c_{C\_2}}. \qquad \text{(A.16)}$$

For Zn^{2+} adsorbed at the rutile (110)–aqueous interface, two ion heights were observed at $z_{C\_1} = 3.16$ Å and $z_{C\_2} = 2.70$ Å. The coherent fractions and positions calculated with both models are shown in Figs. A.3A and A.3B, respectively. Here $c_{\mathrm{EDL}} = c_{C\_1} + c_{C\_2}$ represents the fractional occupation of the condensed-layer ions in the system, where $c_{\mathrm{EDL}} = 1$ means that all ions are in the condensed layer and $c_{\mathrm{EDL}} = 0.5$ means that half of the ions are in the condensed layer; $\sigma_C = 0.1$ Å; and for the one-height model $\overline{z_C} = 3.0$ Å.

As Fig. 6 shows, ion height does not change significantly as ionic strength changes. The constancy of the more weakly bound Sr^{2+} ion height over this ionic strength range supports the assumption that the two Zn^{2+} ion heights did not change in the measurements. Therefore, ion participation between the two sites ($c_{C\_1} : c_{C\_2}$) should be constant to keep the average position fixed.

The coherent fractions calculated with the two-height model are always lower than those from the one-height model, but the difference is less than 10%. This means that the actual Stern coverage in the two-height case could be higher by ~10% than the number derived from the measured coherent fractions by using the one-height model. As Fig. A.3 clearly shows, changes in the degree of partitioning of ions between the condensed layer

and other sources affect only the coherent fractions, not the coherent positions.

When the diffuse-layer and bulk-solution ions are included, the earlier discussions about the GC and the GCS model remain valid when Zn^{2+} ions have two heights. However, in this situation more parameters must be taken into consideration in calculations of the coherent fraction and position.

References

[1] W. Stumm, L. Sigg, B. Sulzberger, Chemistry of the Solid–Water Interface: Processes at the Mineral–Water and Particle–Water Interface in Natural Systems, Wiley, New York, 1992.
[2] G.E. Brown, V.E. Henrich, W.H. Casey, D.L. Clark, C. Eggleston, A. Felmy, D.W. Goodman, M. Gratzel, G. Maciel, M.I. McCarthy, K.H. Nealson, D.A. Sverjensky, M.F. Toney, J.M. Zachara, Chem. Rev. 99 (1999) 77.
[3] G.E. Brown, G.A. Parks, Int. Geol. Rev. 43 (2001) 963.
[4] G. Gouy, J. Phys. 9 (1910) 457.
[5] D.L. Chapman, Philos. Mag. 25 (1913) 475.
[6] O.H. Stern, Z. Elektrochem. 30 (1924) 52.
[7] T. Hiemstra, P. Venema, W.H.V. Riemsdijk, J. Colloid Interface Sci. 184 (1996) 680.
[8] T. Hiemstra, W.H. Van Riemsdijk, J. Colloid Interface Sci. 179 (1996) 488.
[9] M.L. Machesky, D.J. Wesolowski, D.A. Palmer, K. Ichiro-Hayashi, J. Colloid Interface Sci. 200 (1998) 298.
[10] D.A. Sverjensky, Geochim. Cosmochim. Acta 65 (2001) 3643.
[11] R. Charmas, J. Phys. Chem. B 106 (2002) 9059.
[12] M.K. Ridley, M.L. Machesky, D.J. Wesolowski, D.A. Palmer, Geochim. Cosmochim. Acta 69 (2005) 63.
[13] M.K. Ridley, M.L. Machesky, D.J. Wesolowski, D.A. Palmer, Geochim. Cosmochim. Acta 63 (1999) 3087.
[14] M.V. Fedkin, X.Y.Y. Zhou, J.D. Kubicki, A.V. Bandura, S.N. Lvov, M.L. Machesky, D.J. Wesolowski, Langmuir 19 (2003) 3797.
[15] M.J. Bedzyk, G.M. Bommarito, M. Caffrey, T.L. Penner, Science 248 (1990) 52.
[16] J. Wang, M. Caffrey, M.J. Bedzyk, T.L. Penner, Langmuir 17 (2001) 3671.
[17] G.D. Williams, A.K. Soper, N.T. Skipper, M.V. Smalley, J. Phys. Chem. B 102 (1998) 8945.
[18] T. Hiemstra, W.H. Vanriemsdijk, G.H. Bolt, J. Colloid Interface Sci. 133 (1989) 91.
[19] P. Fenter, Mineral. Soc. Am. 49 (2002) 149.
[20] P. Fenter, L. Cheng, S. Rihs, M. Machesky, M.J. Bedzyk, N.C. Sturchio, J. Colloid Interface Sci. 225 (2000) 154.
[21] P. Fenter, N.C. Sturchio, Prog. Surf. Sci. 77 (2004) 171.
[22] P.J. Eng, T.P. Trainor, G.E. Brown, G.A. Waychunas, M. Newville, S.R. Sutton, M.L. Rivers, Science 288 (2000) 1029.
[23] L. Cheng, P. Fenter, K.L. Nagy, M.L. Schlegel, N.C. Sturchio, Phys. Rev. Lett. 8715 (2001).
[24] M.L. Schlegel, K.L. Nagy, P. Fenter, N.C. Sturchio, Geochim. Cosmochim. Acta 66 (2002) 3037.
[25] K.F. Hayes, A.L. Roe, G.E. Brown, K.O. Hodgson, J.O. Leckie, G.A. Parks, Science 238 (1987) 783.
[26] J.R. Bargar, S.N. Towle, G.E. Brown, G.A. Parks, J. Colloid Interface Sci. 185 (1997) 473.
[27] S.N. Towle, G.E. Brown, G.A. Parks, J. Colloid Interface Sci. 217 (1999) 299.
[28] T.P. Trainor, J.P. Fitts, A.S. Templeton, D. Grolimund, G.E. Brown, J. Colloid Interface Sci. 244 (2001) 239.
[29] T.P. Trainor, A.S. Templeton, G.E. Brown, G.A. Parks, Langmuir 18 (2002) 5782.
[30] Z. Zhang, P. Fenter, L. Cheng, N.C. Sturchio, M.J. Bedzyk, M.L. Machesky, D.J. Wesolowski, Surf. Sci. 554 (2004) L95.
[31] Z. Zhang, P. Fenter, L. Cheng, N.C. Sturchio, M.J. Bedzyk, M. Predota, A. Bandura, J.D. Kubicki, S.N. Lvov, P.T. Cummings, A.A. Chialvo, M.K. Ridley, P. Benezeth, L. Anovitz, D.A. Palmer, M.L. Machesky, D.J. Wesolowski, Langmuir 20 (2004) 4954.
[32] M.K. Ridley, M.L. Machesky, D.A. Palmer, D.J. Wesolowski, Colloids Surf. A 204 (2002) 295.
[33] A.V. Bandura, J.D. Kubicki, J. Phys. Chem. B 107 (2003) 11072.
[34] A.V. Bandura, D.G. Sykes, V. Shapovalov, T.N. Troung, J.D. Kubicki, R.A. Evarestov, J. Phys. Chem. B 108 (2004) 7844.
[35] M. Predota, A.V. Bandura, P.T. Cummings, J.D. Kubicki, D.J. Wesolowski, A.A. Chialvo, M.L. Machesky, J. Phys. Chem. B 108 (2004) 12049.
[36] M. Predota, Z. Zhang, P. Fenter, D.J. Wesolowski, P.T. Cummings, J. Phys. Chem. B 108 (2004) 12061.
[37] M.J. Bedzyk, L.W. Cheng, Mineral. Soc. Am. 49 (2002) 221.
[38] B.W. Batterman, Phys. Rev. Lett. 22 (1969) 703.
[39] J.A. Golovchenko, J.R. Patel, D.R. Kaplan, P.L. Cowan, M.J. Bedzyk, Phys. Rev. Lett. 49 (1982) 560.
[40] J. Zegenhagen, Surf. Sci. Rep. 18 (1993) 202.
[41] L. Cheng, P. Fenter, M.J. Bedzyk, N.C. Sturchio, Phys. Rev. Lett. 90 (2003) 255503.
[42] J.S. Okasinski, C.-Y. Kim, D.A. Walko, M.J. Bedzyk, Phys. Rev. B 69 (2004) 041401.
[43] V.E. Henrich, P.A. Cox, The Surface Science of Metal Oxides, Cambridge Univ. Press, Cambridge/New York, 1994.
[44] U. Diebold, Surf. Sci. Rep. 48 (2003) 53.
[45] G. Charlton, P.B. Howes, C.L. Nicklin, P. Steadman, J.S.G. Taylor, C.A. Muryn, S.P. Harte, J. Mercer, R. McGrath, D. Norman, T.S. Turner, G. Thornton, Phys. Rev. Lett. 78 (1997) 495.
[46] S. Takakusagi, K.-i. Fukui, F. Nariyuki, Y. Iwasawa, Surf. Sci. 523 (2003) L41.
[47] R.M. Garrels, C.L. Christ, Solutions, Minerals, and Equilibria, Harper & Row, New York, 1965.
[48] H. Tamura, N. Katayama, R. Furuichi, J. Colloid Interface Sci. 195 (1997) 192.
[49] J.R. Bargar, G.E. Brown, G.A. Parks, Geochim. Cosmochim. Acta 62 (1998) 193.
[50] J.R. Bargar, R. Reitmeyer, J.J. Lenhart, J.A. Davis, Geochim. Cosmochim. Acta 64 (2000) 2737.
[51] R. Rietra, T. Hiemstra, W.H. Van Riemsdijk, Environ. Sci. Technol. 35 (2001) 3369.
[52] P.C. Hiemenz, R. Rajagopalan, Principles of Colloid and Surface Chemistry, Dekker, New York, 1997.
[53] C.J. Howard, T.M. Sabine, F. Dickson, Acta Crystallogr. B 47 (1991) 462.